Bulletin of the Geological Society of Malaysia, Volume 82, November 2026, pp. 33 - 43
DOI: https://doi.org/10.7186/bgsm82202604

Comparative evaluation of helically wound fibre wrapping angle for distributed acoustic sensing subsurface imaging

Rifqi Roid Dhiaulhaq*, Siti Nur Fathiyah Jamaludin, Khairul Arifin Mohd Noh, Abdul Rahim Md Arshad

Centre for Subsurface Imaging, Department of Geosciences, Universiti Teknologi PETRONAS, 32610 Seri Iskandar, Perak, Malaysia
*Corresponding author email address: rifqi_24004159@utp.edu.my

Abstract: Distributed acoustic sensing (DAS) represents an emerging technology for subsurface imaging with the potential to replace current seismic technologies. However, DAS applications in reflection seismic imaging are constrained by intrinsic broadside sensitivity limitations. This research examines the imaging potential of DAS helically wound fibre (HWF) configurations with varying wrapping angles for subsurface structure detection via detailed synthetic modelling. This research employs a 2 km section of the Marmousi2 model featuring gas-charged sand channels to evaluate the imaging capabilities of straight fibre and helically wound fibre (HWF) configurations with wrapping angles of 15°, 30°, 45°, 60°, and 75°, in conjunction with conventional seismic horizontal (*Vx*) and vertical (*Vz*) components. Pre-stack depth migration approaches are applied to examine imaging capabilities across different configurations. The results show that HWF configurations with lower wrapping angles (15° and 30°) provide better imaging performance for complex subsurface structures, achieving imaging quality comparable to conventional seismic vertical components. These configurations work well for capturing curved gas-charged sand channel features because of their higher broadside sensitivity (46.7% and 37.5% respectively at $\theta = 90°$). Higher wrapping angles (60° and 75°) display progressively degraded performance, approaching straight fibre characteristics with reduced capabilities to capture complex structures. This research provides information for practitioners in identifying the most suitable helical configurations depending on specific geological targets and survey objectives, therefore enhancing the practical application of DAS technology in exploration geophysics.

Keywords: Distributed acoustic sensing, helically wound fibre, subsurface imaging, wrapping angle, broadside sensitivity

INTRODUCTION

Distributed acoustic sensing (DAS) represents an emerging technology for subsurface imaging with potential advantages over conventional seismic methods, including lower deployment costs, increased flexibility, and higher spatial resolution due to denser channel spacing along fibre optic cables (Zhu *et al*., 2020). The system uses backscattered light analysis along the entire fibre length and continuous laser pulse transmission to measure dynamic strain rates (Pendão & Silva, 2022). Unlike discrete point sensors such as geophones, DAS enables meter or submeter channel spacing for subsurface structure detection, particularly in hydrocarbon exploration (Bakulin *et al*., 2020).

Straight fibre DAS faces significant limitations in the use of DAS in reflection seismic imaging. In contrast to conventional three-component geophones, DAS only offers one-component sensing that is mainly sensitive to waves that propagate parallel to the fibre. It is completely insensitive to broadside waves, which propagate perpendicular to the fibre, and sensitivity to high incidence angles is poor (Masaya *et al*., 2024). This directional dependence follows a $\cos^2 \theta$ sensitivity pattern, where θ represents the incidence angle between seismic waves and fibre direction. Straight fibre configurations cannot perform optimally for subsurface imaging applications because reflection seismic imaging necessitates capturing waves at high incidence angles typical of broadside propagation (Wuestefeld & Wilks, 2019).

Helically wound fibre (HWF) configurations overcome these limitations by winding the cable helically to detect both horizontal and vertical seismic vibration components (Chugaev & Tarantin, 2023). Directional sensitivity characteristics are determined by the wrapping angle, which is the angle at which the fibre is wound around the central axis of the cable. Higher wrapping angles offer better surface wave suppression but lower broadside sensitivity, while lower wrapping angles offer higher broadside sensitivity but reduced surface wave discrimination (Adeniyi *et al*., 2025).

Field validation of HWF notwithstanding, there is still a lack of systematic comparative evaluation of imaging capabilities for particular geological targets across the

0126-6187; 2637-109X / Published by the Geological Society of Malaysia.
© 2026 by the Author(s). This is an open access article distributed under the terms of the Creative Commons Attribution (CC-BY) License 4.0.

entire range of practically feasible wrapping angles. To detect subsurface structures, previous research has mostly concentrated on single wrapping angle implementations without thorough comparison analysis. By systematically comparing the imaging capabilities of straight fibre and HWF configurations with wrapping angles of 15°, 30°, 45°, 60°, and 75° for subsurface structure detection, this study addresses this gap. This study uses detailed synthetic modeling to assess imaging performance using pre-stack depth migration techniques on a 2 km segment of the Marmousi2 model with gas-charged sand channels. The results facilitate the practical deployment of DAS technology in exploration geophysics by giving practitioners guidance in choosing the best helical configurations based on particular geological targets and survey objectives.

Fundamental of distributed acoustic sensing (DAS)

Distributed acoustic sensing (DAS) utilizes fibre optic cables to detect vibrations along the entire cable length, providing continuous spatial sensing capabilities with high spatial and temporal resolution (Fernández-Ruiz *et al*., 2020). DAS uses optical fibre cables as the medium for acquiring seismic data and light as the information carrier. The interrogator unit (IU) and the fibre sensing cable are the two main parts of DAS systems (Pastor-Graells *et al*., 2016).

As shown in Figure 1, the operational principle is based on optical time-domain reflectometry (OTDR), with phase optical time-domain reflectometry (Phase-OTDR) being used to measure dynamic strain (Rashid *et al*., 2025). Laser pulses are continuously sent along the optical fibre cable by the interrogator unit. Backscattered light returns to the interrogator unit as a result of Rayleigh scattering caused by spatial variations in the refractive index during light propagation through the fibre core. The two-way travel time for laser pulses to travel down the fibre and for backscattered light to return to the IU determines the measurement locations (Muanenda, 2018).

The optical phase shift between backscatter components coming from the leading and trailing portions of the optical pulse is changed when acoustic waves or vibrations lengthen the optical fibre (Asfha *et al*., 2024). The detection of acoustic events along the fibre is made possible by these phase changes, which result in variations in the intensity of returning light from one pulse to another. The DAS interrogator unit analyzes the phase information of coherent Rayleigh scattered light to produce measurements of dynamic strain, including vibrations and acoustic waves (Masoudi & Newson, 2016).

Helically wound fibre (HWF) and wrapping angles

Helically wound fibre (HWF) represents a solution in addressing the broadside sensitivity limitations of straight fibre cable (Hornman, 2017). The concept of HWF involves wrapping the optical fibre in a helical pattern, creating a three-dimensional sensing geometry that enhances sensitivity to waves from multiple directions, as illustrated in Figure 2.

As illustrated in Figure 2, the helical configuration modifies the direction of fibre response by introducing components sensitive to both axial and radial wave propagation. When compared to straight fibre deployments, this geometry configuration improves broadside wave detection capabilities by enabling the fibre to capture portions of both horizontal and vertical wave components (Tsuji *et al*., 2025). This improvement is demonstrated by the equation from (Al Hasani & Drijkoningen, 2023), which shows that HWF contains contributions from both horizontal and vertical strain rate components, allowing the acquisition of both horizontal and vertical component measurements. The directional sensitivity characteristics of HWF are determined by the wrapping angle (α), which indicates the angle at which the fibre is wound around the central axis of the cable. The wrapping angle is defined as the angle between the fibre trajectory and the circumference of the cable when the cylindrical surface is flattened onto a horizontal plane (Kuvshinov, 2016).

Different wrapping angles offer different capabilities for capturing waves at different incidence angles, which correspond to their capacity to detect both horizontal and vertical components, as shown in Figure 2. The dynamic strains imposed on an HWF due to acoustic waves create a complex three-dimensional response that depends on both the wrapping geometry and surrounding properties. The wrapping angle controls the sensitivity of the cable, with lower wrapping angles providing higher sensitivity to broadside seismic waves (Chugaev & Kuznetsov, 2023).

Sensitivity in DAS refers to the ratio of the strain measured by the optical fibre to the actual strain induced in

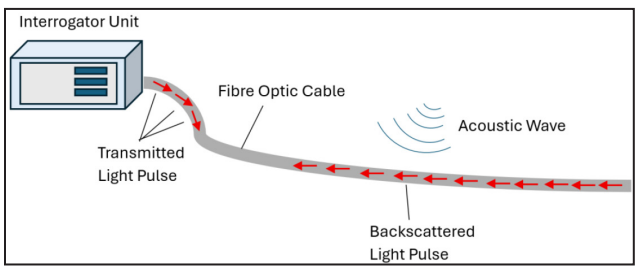


Figure 1: Illustration of distributed acoustic sensing concept based on Optical Time Domain Reflectometry (OTDR) principle.

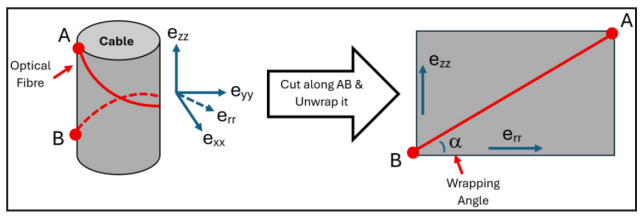


Figure 2: Illustration of wrapping angle in helically wound fibre. Modified after (Hendi *et al*., 2020).

the surrounding medium by seismic waves. This sensitivity is directionally dependent and determines what proportion of the true ground motion can be captured by the fibre sensor. For straight fibre configurations, sensitivity follows a $\cos^2\theta$ relationship, where θ represents the incidence angle between the seismic wave propagation direction and the fibre axis (Mateeva *et al*., 2014; Kuvshinov, 2016). For HWF configurations, the sensitivity depends on both the incidence angle and the wrapping angle, as expressed in the following equation (Kuvshinov, 2016):

$$\cos^2\theta \sin^2\alpha + \frac{\sin^2\theta \cos^2\alpha}{2} \quad (1)$$

Where θ is the angle of incidence, α is the cable's wrapping angle. For the perpendicular incidence angle (θ = 90°), the broadside sensitivity simplifies to the expression given in Equation 2 (Kuvshinov, 2016):

$$\varepsilon HWF = \frac{\cos^2\alpha}{2} \quad (2)$$

Equation 2 illustrates that varying wrapping angles provide variable broadside sensitivity, as detailed in Table 1.

To populate Table 1, we applied Equation 1 across different wrapping angles (α = 0°, 15°, 30°, 45°, 60°, 75°, and 90°) and wave incidence angles (θ = 0°, 30°, 60°, and 90°). Each sensitivity value indicates how much of the ground strain the HWF can detect relative to a straight fibre responding to a parallel wave which represents the maximum measurable strain in conventional DAS (Kuvshinov, 2016). As an example for a wrapping angle of 30° at perpendicular incidence (θ = 90°), substituting into Equation 1:

$$\cos^2 90°\sin^2 30° + \frac{\sin^2 90° \cos^2 30°}{2} = 0 + \frac{(1 \text{ x } 0.75)}{2}$$

$$= 0.375 \quad (3)$$

This calculation yields the 37.5% broadside sensitivity shown in Table 1.

Table 1 reveals how different wrapping angles impact broadside sensitivity at different wave incidence angles. The values, which included both broadside and parallel waves (θ = 0°), were computed using Equation 1 to investigate sensitivity across wrapping angles and wave incidence angles. The results show that the design of HWFs involves a fundamental trade-off. Lower wrapping angles (15°-30°) show less sensitivity to parallel waves (θ = 0°) but provide improved sensitivity to broadside waves (θ = 90°). Higher wrapping angles (60° to 90°), on the other hand, show better sensitivity to parallel waves but significantly worse performance for broadside wave detection. The significance of selecting appropriate wrapping angles based on specific seismic survey requirements and target wave propagation characteristics is highlighted by this inverse relationship (Adeniyi *et al*., 2025).

It is important to note that the enhanced broadside sensitivity of HWF configurations cannot be attributed to the increased fibre length per unit cable length. While Table 2 shows that lower wrapping angles require more fibre, the sensitivity enhancements arise from geometric strain decomposition mechanism. The fibre longitudinal strain in HWF is given by:

$$e^{(f)}_{zz} = e^{(c)}_{ll} \sin^2\alpha + [e^{(c)}_{rr}] \cos^2\alpha \quad (4)$$

Where $e^{(c)}_{11}$ represents cable axial strain and $[e^{(c)}_{rr}]$ represents averaged radial strain. This tensor transformation enables HWF to capture radial cable deformations caused by broadside waves. The helical geometry essentially converts the radial expansion and contraction of the cable, movements that would be invisible to a straight fibre, into measurable changes in fibre length.

The helical winding geometry introduces a relationship between the mandrel diameter and fibre length. When the cylindrical cable surface is unwrapped, it forms a rectangle with the fibre lying along its diagonal. The fibre length (L) relates to the cable circumference ($a = 2\pi R$, where R is the mandrel radius) and axial height (h) through

$$L^2 = \alpha^2 + h^2 \quad (5)$$

Consequently, the fibre length per unit cable length follows the relationship:

$$\frac{L_{fibre}}{L_{cable}} = \frac{1}{\sin\alpha} \quad (6)$$

Table 1: Sensitivities value of various wrapping angles and incidence wave angles.

Wrapping Angle	Broadside Wave (θ = 90°)	Broadside Wave (θ = 60°)	Broadside Wave (θ = 30°)	Parallel Wave (θ = 0°)
15°	46.7 %	36 %	16.7 %	6.7 %
30°	37.5 %	34.3 %	28.1 %	25 %
45°	25 %	31.25 %	43.75 %	50 %
60°	12.5 %	28.125 %	59.38 %	75 %
75°	3.34 %	25.83 %	70.8 %	93.3 %
90°	0 %	25 %	75 %	100 %

Table 2: Fibre length ratio for different wrapping angles in HWF.

Wrapping Angle (α)	Fibre Length Ratio (1/sin α)	Fibre Length Increase (%)
15°	3.86	286 %
30°	2.00	100 %
45°	1.41	41 %
60°	1.15	15 %
75°	1.04	4 %
90° (straight)	1.00	0 %

Where L_{fibre} is the total fibre length, L_{cable} is the cable's axial length, and α is the wrapping angle. Table 2 quantifies these ratios for each wrapping angle configuration, demonstrating that lower wrapping angles translate directly to greater fibre requirements per unit cable length. Commercial helically wound cables typically have diameters ranging from 25 to 33 mm (Hendi *et al*., 2020). The larger cable diameter compared to straight fibre cables is necessary to preserve the waveguide geometry and prevent excessive fibre bending that could degrade optical signal quality (Willis, 2022).

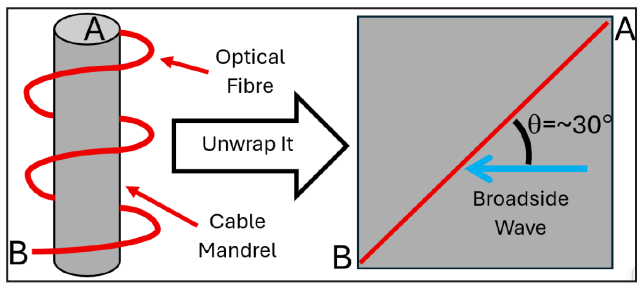


Figure 3: Broadside wave in helically wound fibre (HWF) configuration. Adapted from (Hendi *et al*., 2020).

Broadside wave sensitivity of helically wound fibre

The three-dimensional geometry of HWF configurations allows them to overcome broadside sensitivity constraints. As shown in Figure 3, the helical winding offers fibre segments oriented at different angles with respect to incident waves, making it possible to identify wave components that would be missed by straight fibre deployment (Yavuz *et al*., 2019).

The higher broadside sensitivity seen in Figure 3 derives from the helical geometry's capacity to divide incident waves into components aligned with various fibre segments, therefore allowing the capture of high incidence angle waves. However, helically wound fibres show varied characteristics depending on their wrapping angles. As illustrated by the sensitivity values in Table 1, lower wrapping angles (15°-30°) provide stronger broadside sensitivity but less surface wave discrimination, whereas higher wrapping angles (60°-75°) offer superior surface wave suppression but lower broadside sensitivity (Baird, 2020).

Recent advances and applications

A theoretical framework demonstrates that helically wound fibre broadside sensitivity at perpendicular incidence ($\theta = 90°$) follows Equation 2, where α is the wrapping angle. This suggests that lower wrapping angles result in greater broadside sensitivity but reduced surface wave discrimination (Kuvshinov, 2016). Previous study provided the first field validation through controlled experiments in shallow horizontal boreholes, quantitatively confirming the predicted angle-dependent behaviour and enhanced broadside sensitivity compared to straight fibre configurations (Hornman, 2017). Field tests comparing straight and helically wound fibres with 30° and 60° wrapping angles buried at a depth of 2 meters were carried out in Groningen, the Netherlands (Al Hasani & Drijkoningen, 2023). Helical winding dampens surface waves while preserving P-wave information above 55 Hz, which demonstrated 10–12 dB amplitude increases for helical configurations in P-wave reflections. The study confirmed wrapping angle effects on surface-wave polarity reversal, with straight fibre showing better shallow sensitivity and helically wound fibre superior deeper performance.

For borehole applications, (Mateeva *et al*., 2014) demonstrated DAS effectiveness for reservoir monitoring through vertical seismic profiling with dense spatial sampling. At the Cu-Au New Afton porphyry deposit, DAS showed capabilities for imaging mineralization structures and geological interfaces (Bellefleur *et al*., 2020). Modelling and field research showed that cable coupling and surrounding media characteristics have a significant impact on helically wound fibre performance, weak coupling results in weak amplitudes in helically wound fibre while having little effect on data from straight fibre (Hendi *et al*., 2020). In the East China Sea, 3D DAS-VSP survey was conducted using fibre cables positioned at depths of 3580 and 3170 meters. The survey validated offshore subsurface evaluation capabilities and showed better signal-to-noise ratios than conventional streamer data (Chen *et al*., 2023).

Current research has not systematically compared imaging performance across the full range of feasible wrapping angles (15° - 75°) for specific geological targets. Most studies examine single configurations without establishing relative performance benchmarks against conventional seismic. This study addresses that gap. Adeniyi *et al*. (2025) reviewed innovative cable configurations that address broadside sensitivity limitations and proposed

design improvements (Adeniyi *et al*., 2025), while Rafi *et al*. (2024) demonstrated single-mode fibre superiority over multi-mode fibre for DAS acquisition in most applications (Rafi *et al*., 2024). Neither study provides practical guidelines for selecting optimal wrapping angles based on subsurface imaging objectives, a gap that becomes particularly significant when targeting gas-charged formations in hydrocarbon exploration. This study addresses that gap through comparative investigation of imaging capabilities across helical fibre configurations (15°, 30°, 45°, 60°, and 75° wrapping angles), benchmarked against conventional seismic.

METHODOLOGY

This section explains the techniques used in this study, including dataset selection, acquisition layout design, forward modelling approach, strain-rate conversion, and imaging procedures. The approach uses pre-stack depth migration analysis and synthetic modeling to allow for controlled assessment of DAS imaging capabilities.

Dataset and acquisition layout

For this synthetic seismic imaging study, we selected the Marmousi2 acoustic model as our test bed. Martin *et al*. (2006) developed Marmousi2 as an elastic extension of the original Marmousi model, offering complete subsurface models including P-wave velocity (Vp), S-wave velocity (Vs), and density. The full model extends 17 km laterally and reaches 3.5 km in depth, with 199 geological layers and a 450 m water layer designed to represent deep-water conditions (Martin *et al*., 2006). While these comprehensive elastic parameters exist within the Marmousi2 dataset, we chose to employ only the P-wave velocity and density models for acoustic forward modelling. This decision reflects the dominant role of P-wave reflection imaging in marine seismic exploration for detecting subsurface structures, and allows us to make direct comparisons between DAS configurations and the conventional vertical seismic component (Vz). Our analysis therefore focuses on P-wave propagation and imaging, intentionally excluding S-wave and converted wave phenomena. We extracted a 2 km section from the model's first phase containing gas-charged sand channel structures, features that present exactly the kind of complex geological targets needed to properly evaluate DAS imaging capabilities, particularly for helically wound fibre topologies. Figure 4 shows the density model for this 2 km section, which spans 2 km laterally, extends to 1900 m depth, and includes a 460 m water layer.

Given the presence of a water layer in the Marmousi2 model, we employed an ocean bottom cable (OBC) acquisition geometry where receivers sit at the seafloor while seismic sources operate at the ocean surface (Noh *et al*., 2015). To maintain consistent subsurface illumination, we used a 10 m source interval for both conventional seismic and DAS simulations. For conventional seismic recording, we adopted a 10 m receiver interval that mirrors typical geophone spacing in marine surveys. DAS recording, however, leverages the inherent high spatial resolution of fibre optic technology by employing a 1.25 m receiver interval. DAS datasets are generated by converting conventional seismic particle velocity data acquired at 1.25 m receiver spacing to strain rate measurements.

Selecting an appropriate gauge length in DAS systems means navigating an inherent trade-off between sensitivity and spatial resolution. Longer gauge lengths enhance strain sensitivity through increased optical phase averaging, which improves signal-to-noise ratio but comes at the cost of reduced spatial resolution. Conversely, shorter gauge lengths offer better spatial resolution but with lower sensitivity. For this study, the gauge length was set equal to the channel spacing (1.25 m). It preserved the spatial resolution already built into our channel configuration, and it allowed us to isolate the effects of wrapping angle without introducing gauge length as a confounding variable.

The acquisition geometry and synthetic modelling parameters used for the conventional seismic and DAS simulations are summarized in Table 3.

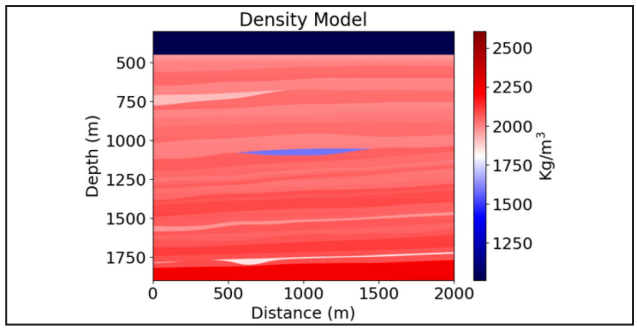


Figure 4: Density model of 2km section of the Marmousi2 model.

Table 3: Acquisition parameters for synthetic seismic simulations.

Parameter	Conventional Seismic	DAS
Acquisition geometry	Ocean bottom cable (OBC)	
Source position	Sea surface	
Receiver position	Seafloor	
Source interval	10 m	10 m
Receiver interval	10 m	1.25 m

The gauge length selection was validated based on spatial sampling requirements derived from seismic wavelengths present in the Marmousi2 model. The minimum wavelength we needed to capture is calculated as:

$$\lambda_{min} = \frac{V_{min}}{f_{max}} = \frac{1500\ m/s}{30\ Hz} = 50\ m \quad (7)$$

Where V_{min} = 1500 m/s represents the P-wave velocity in the water layer (the slowest velocity in our acoustic model), while f_{max} = 30 Hz corresponds to the maximum frequency content of the Ricker wavelet source. To prevent spatial aliasing, the Nyquist criterion requires that:

$$GL \leq \frac{\lambda_{min}}{2} = \frac{50\ m}{2} = 25\ m \quad (8)$$

The selected gauge length of 1.25 m satisfies this criterion with a factor of 20 margin, ensuring that the full frequency content of the seismic wavefield is captured without spatial aliasing or signal attenuation.

Research workflow

The research workflow consists of forward modelling of the 2 km section of the Marmousi2 model, converting particle velocity to strain rate, processing datasets, and pre-stack depth migration, as illustrated in Figure 5. The Datasets including conventional seismic horizontal (Vx) and vertical (Vz) components, straight fibre, and HWF with 15°, 30°, 45°, 60°, and 75° wrapping angles follow identical processing to ensure consistent treatment. The final output generates pre-stack depth migration images for comparative analysis. The migrated DAS images are compared with the density model and conventional seismic images to examine DAS capabilities for subsurface imaging. Conventional seismic is chosen for comparison as it is a proven method for subsurface seismic imaging.

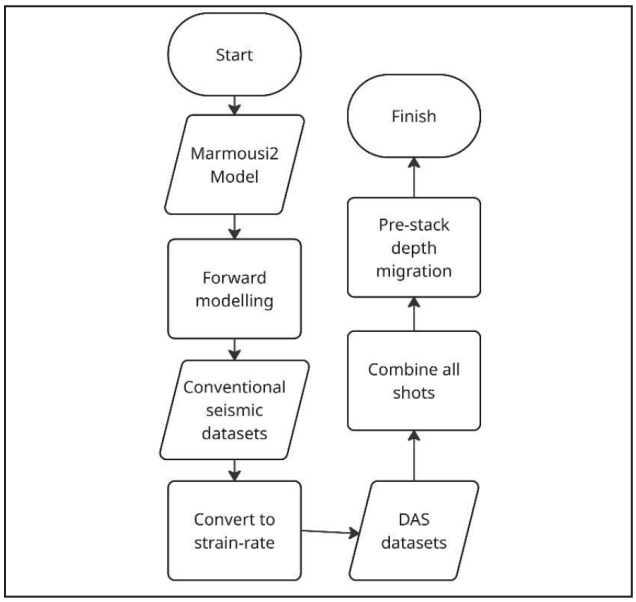


Figure 5: Research workflow.

Particle velocity to strain rate conversion

Particle velocity data must be converted to strain rate measurements in order to create DAS datasets. For conventional DAS measurements, the conversion from particle velocity to strain rate follows the relationship established by (Willis, 2022):

$$\dot{\varepsilon}_{zz} = \frac{V_z(z + GL/2) - V_z(z - GL/2)}{GL} \quad (9)$$

where $\dot{\varepsilon}_{zz}$ represents the vertical strain rate measured by DAS, V_z represents particle velocity in the vertical direction, z represents the measurement location, and GL specifies the gauge length. This formula applies centered finite differences that are uniformly distributed around every measurement point (Willis, 2022).

Helically wound fibre response calculation

For helically wound fibre configurations, strain rate calculation requires incorporation of wrapping angle parameters using the equation by (Al Hasani & Drijkoningen, 2023):

$$\begin{pmatrix} \varepsilon_{SF} \\ \varepsilon_{HWF} \end{pmatrix} = \begin{pmatrix} 1 & 0 \\ \sin^2\alpha & \cos^2\alpha \end{pmatrix} \begin{pmatrix} \dot{\varepsilon}_{xx} \\ \dot{\varepsilon}_{zz} \end{pmatrix} \quad (10)$$

where ε_{SF} represents straight fibre strain rate, ε_{HWF} represents helically wound fibre strain rate, α represents the wrapping angle, $\dot{\varepsilon}_{xx}$ represents the horizontal strain rate component (spatial partial derivative of horizontal particle velocity), and $\dot{\varepsilon}_{zz}$ represents the vertical strain rate component (spatial partial derivative of vertical particle velocity). With different sensitivities based on the wrapping angle, this formulation allows helically wound fibres to capture both horizontal and vertical seismic wave components. DAS datasets for straight and helically wound fibre configurations with wrapping angles of 15°, 30°, 45°, 60°, and 75° are produced using these conversion equations. Conventional seismic datasets for horizontal (Vx) and vertical (Vz) components are reserved for comparative analysis.

Pre-stack depth migration (Pre-SDM)

Pre-SDM processes unstacked CMP gathers to preserve the complete range of source-receiver offsets and amplitude information (Ziramov *et al*., 2023). The migration accounts for complex wavefield propagation through lateral velocity variations by precisely placing reflection events in depth using the Marmousi2 velocity model. This approach provides optimal imaging resolution and effectively images steep structural dips and complex geological features, making it suitable for imaging the gas-charged sand channels present

in the Marmousi2 model. In order to select the best fibre configuration for real-world deployment scenarios, the implementation allows for a thorough evaluation of how various DAS configurations perform when imaging involved subsurface structures.

RESULTS

This section presents the results of migrated images and discusses the findings to analyze the capabilities of DAS compared to density and conventional seismic images. The results of migrated images consist of pre-stack in depth and distance domain with datasets of conventional seismic horizontal (*Vx*) and vertical (*Vz*) component, straight fibre, and HWF with wrapping angles of 15°, 30°, 45°, 60°, and 75°.

Pre-stack depth migration results

Figure 6 demonstrates imaging performance differences among conventional seismic vertical (*Vz*), horizontal (*Vx*) components, straight fibre, and the reference density model. All images share identical depth and distance coordinates, enabling direct comparison. The density model serves as validation reference, displaying lithological contrasts, particularly the gas-charged sand channel feature shown in blue at approximately 1000-1200 m depth. Migrated images were normalized to enable comparative analysis.

Vertical component of conventional seismic (*Vz*) successfully captures seismic reflections from both upper and lower portions of the gas-charged sand channel, providing complete structural imaging. Conversely, horizontal component of conventional seismic *(Vx*) exhibits limited performance, capturing only the lower portion while failing to image the upper curved section. Similarly, straight fibre captures only the lower part of the gas-charged sand channel but cannot capture the upper curved section. For seafloor boundary imaging, straight fibre exhibits thick reflection characteristics similar to *Vx*, compared to *Vz* which captures the seafloor boundary clearly. Straight fibre also cannot capture reflections below 1250 m depth and displays lower amplitude compared to conventional seismic images. Despite these limitations, straight fibre manages to capture the lower part of the gas feature with performance comparable to *Vx*.

Figure 7 presents pre-stack depth migrated images of HWF with wrapping angles of 15°, 30°, 45°, 60°, and 75° compared to *Vz*. *Vz* is selected for comparison as a proven method for subsurface imaging, and HWF is comparable to *Vz* because it contains portions of vertical strain rate components from its conversion (Equation 4). *Vz* successfully captures complete seismic reflection of the gas-charged sand channel with clear reflection of both upper and lower portions.

HWF 15° and 30° configurations produce the clearest images, successfully capturing both the complete gas-charged sand channel structure (upper and lower portions) and seafloor reflections. HWF 15° demonstrates the cleanest reflection quality among all configurations, with sharp

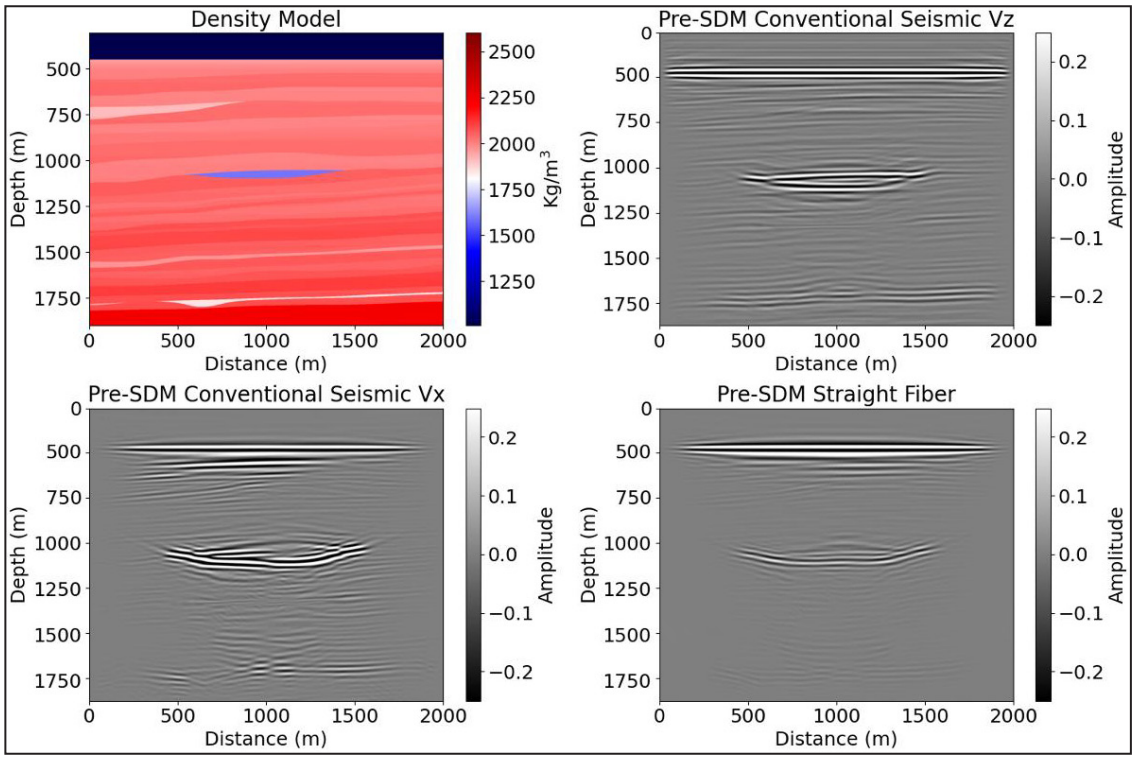


Figure 6: Comparison of pre-stack depth migration of vertical component of conventional seismic (*Vz*), horizontal component of conventional seismic (*Vx*), and straight fibre with density model.

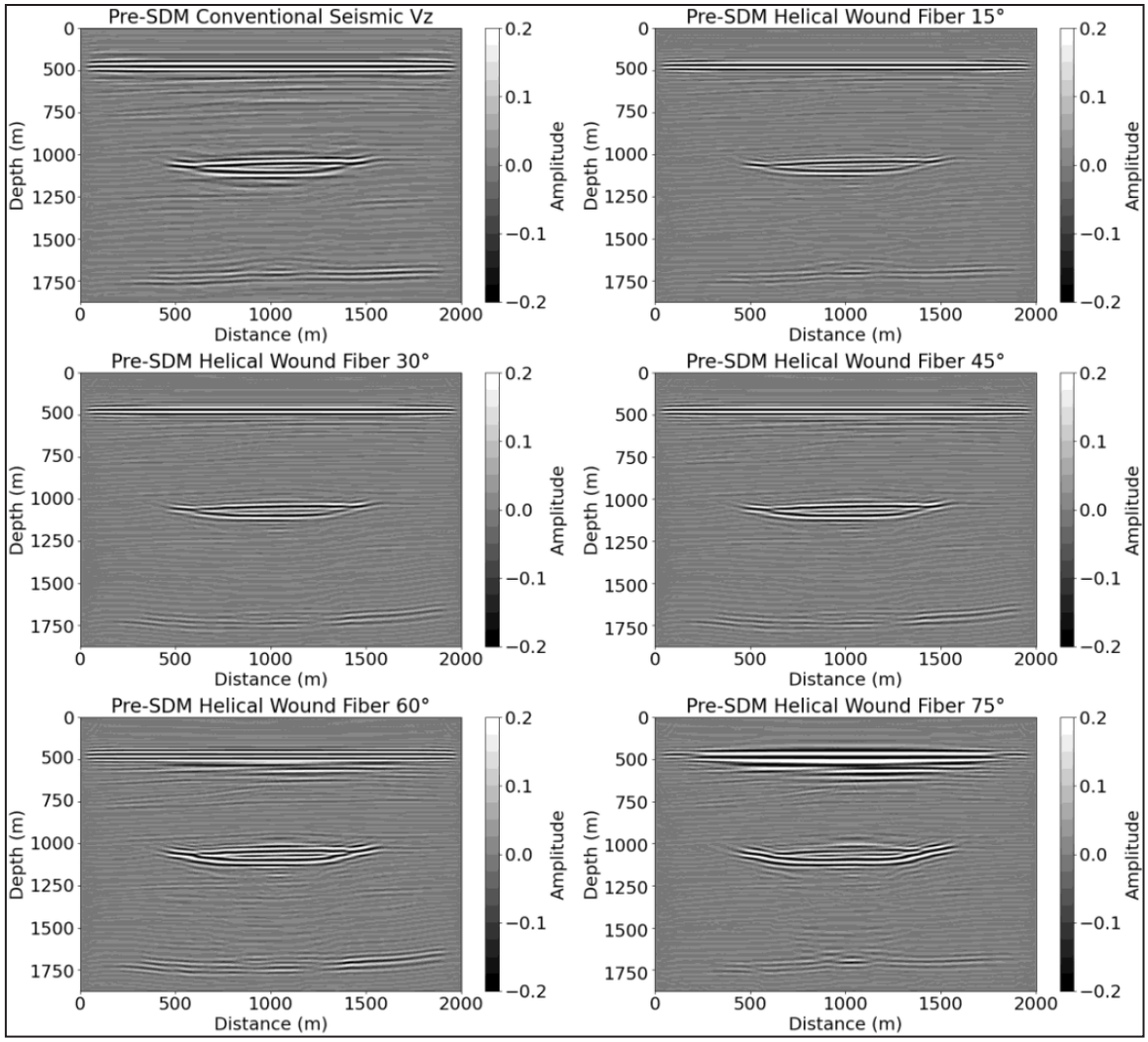


Figure 7: Comparison of pre-stack depth migration of HWF with wrapping angles of 15°, 30°, 45°, 60°, and 75° with vertical component of conventional seismic (*Vz*).

imaging of the curved gas channel geometry that matches the density model structure. HWF 30° maintains similar capabilities for capturing the complete seismic reflection of the gas-charged sand channel, though with slightly reduced clarity compared to HWF 15°. HWF 45° configuration captures the gas feature with clarity approaching that of 15° and 30° configurations, successfully imaging both upper and lower portions visible in the density model. However, HWF 45° begins to display thicker seafloor reflections compared to lower wrapping angles, indicating onset of compromised imaging performance for horizontal boundaries.

HWF 60° configuration exhibits noticeably degraded performance, producing thicker reflections at both the gas feature and seafloor boundary. While the configuration still captures the general structure of the gas-charged sand channel visible in the density model (Figure 6), the reflection quality shows significant deterioration with loss of sharpness in imaging the curved geometry. HWF 75° configuration demonstrates severely compromised imaging capabilities. The configuration shows very thick seafloor reflection from 450 m to 600 m depth, indicating lost capability to capture reflections from horizontal boundaries. Most critically, HWF 75° begins to lose ability to capture the upper curved portion of the gas-charged sand channel at 1050 m depth. This failure to image curved features exhibits characteristics similar to conventional seismic *Vx*.

DISCUSSION

The systematic performance differences observed in Figure 7 directly correlate with the strain rate composition of each HWF configuration as defined by Equation 4. The enhanced imaging capabilities of HWF 15° and 30° configurations derive from their higher content of vertical strain rate component ($\dot{\varepsilon}_{zz}$). With $\theta = 90°$, the broadside sensitivity of 15° is 46.7%, while sensitivity of 30° is 37.5% (Table 1, calculated using Equation 2). Equation 9 states that the spatial partial derivative of the vertical particle velocity component (*Vz*) from conventional seismic data is used to

calculate the vertical strain rate (Willis, 2022). *Vz* has proven effective for capturing high incidence angle reflections and deep subsurface features, including gas-charged formations and structures with curved geometries or steep angles. Consequently, HWF configurations incorporating higher proportions of vertical strain rate components inherit these proven imaging capabilities for complex geological structures.

HWF 45° exhibits a balanced yet transitional sensitivity pattern, maintaining 25% broadside sensitivity at θ = 90° and increasing to 50% sensitivity for parallel waves at θ = 0° (Table 1). This explains the beginning of thicker seafloor reflections observed in the results, as the configuration begins to lose optimal sensitivity to high-angle broadside waves characteristic of horizontal boundaries. The degraded performance of HWF 60° occurs because the portion of vertical strain rate component ($\dot{\varepsilon}_{zz}$) decreases to 12.5% broadside sensitivity while the horizontal strain rate component ($\dot{\varepsilon}_{xx}$) increases to 75% parallel wave sensitivity (Table 1). This shift in sensitivity profile renders the configuration progressively less suitable for imaging curved structures that produce high-angle broadside reflections. The imaging capabilities of HWF 75° are severely compromised for both seafloor boundaries and curved gas channel structures due to its extremely limited broadside sensitivity (3.34% at θ = 90°) and high parallel wave sensitivity (93.3% at θ = 0°). Higher wrapping angles progressively approach straight fibre characteristics that contain only horizontal strain rate component ($\dot{\varepsilon}_{xx}$), as described by Table 1.

HWF configurations of DAS exhibit distinct sensitivity characteristics that depend on the wrapping angle geometry. Figure 8 illustrates the physical configuration of HWF with wrapping angles of 15°, 30°, 45°, 60°, 75°, and 90° (straight fibre), showing how the helical winding pattern varies across these configurations. Lower wrapping angle (15°–30°) results in denser helical winding around the cable mandrel, which geometrically translates to increased sensitivity to broadside waves. Table 1 shows that HWF with a 15° wrapping angle achieves 46.7% broadside sensitivity at perpendicular incidence (θ = 90°), while a 30° wrapping angle yields 37.5% broadside sensitivity, as determined by Equation 2. This enhanced broadside sensitivity makes lower wrapping angle configurations effective for capturing curved geological structures such as gas-charged sand channels, which generate high-angle broadside reflections. Conversely, higher wrapping angles (60°-75°) exhibit progressively looser helical winding patterns that increasingly approximate straight fibre geometry. This geometric transition correlates with reduced broadside sensitivity, 60° wrapping angle provides only 12.5% broadside sensitivity, while 75° provides merely 3.34% at θ = 90° (Table 1). However, these higher wrapping angle configurations demonstrate enhanced sensitivity to parallel waves (75% for 60° and 93.3% for 75° at θ = 0°), approaching the characteristics of straight fibre (90°), which exhibits 100% sensitivity to parallel waves and 0% to broadside waves (Kuvshinov, 2016). The imaging capabilities of various HWF configurations for subsurface structural detection are essentially determined by this inverse relationship between wrapping angle magnitude and broadside wave sensitivity.

Figure 9 presents calculated sensitivity for each wrapping angle configuration using Equation 1, which considers both wrapping fibre angle and incidence angle (Kuvshinov, 2016). HWF 15° exhibits a lower sensitivity to parallel waves (6.7% at θ = 0°) and an optimal sensitivity to high-angle broadside waves (46.7% at θ = 90°). The 15° configuration is especially useful for imaging curved structures (gas-charged sand channels) which primarily produce high-angle broadside reflections, because of its sensitivity pattern.

HWF 30° exhibits decreased sensitivity to parallel waves (25% at θ = 0°) but retains exceptional sensitivity to high-angle broadside waves (37.5% at θ = 90°). The 45° configuration provides moderate detection capabilities for both broadside and parallel wave types, with balanced sensitivity characteristics (25% at θ = 90°, 50% at θ = 0°). With 60° exhibiting 75% parallel wave sensitivity and only 12.5% broadside sensitivity, and 75° exhibiting 93.3% parallel wave sensitivity with only 3.34% broadside sensitivity, higher wrapping angles show progressive trends toward parallel wave sensitivity. HWF configurations at 0° and 90° cannot strictly be defined as helically wound fibres. According to Equation 4, HWF 90° represents straight fibre utilizing only horizontal strain rate component ($\dot{\varepsilon}_{xx}$),

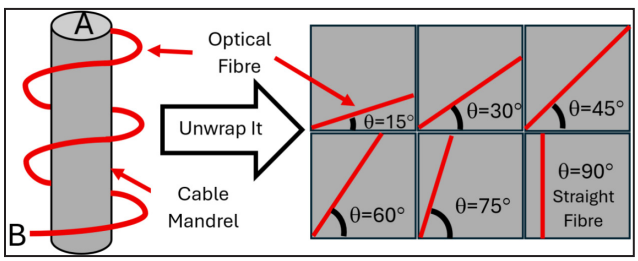


Figure 8: Illustration of HWF wrapping angle and straight fibre. Adapted from (Kuvshinov, 2016).

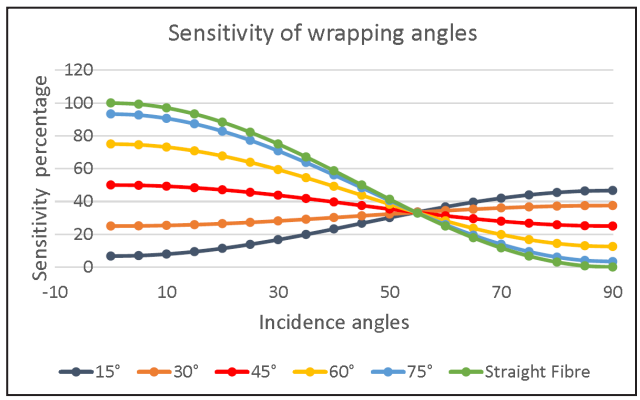


Figure 9: Sensitivity of HWF with wrapping angles of 15°, 30°, 45°, 60°, 75°, and straight fibre.

comparable to conventional seismic horizontal component (Vx). HWF 0° utilizes only vertical strain rate component ($\dot{\varepsilon}_{zz}$), corresponding to conventional seismic vertical component (Vz).

Wrapping angle selection represents a fundamental trade-off between broadside wave sensitivity and parallel wave detection capabilities. Lower wrapping angles (15°-30°) are optimal for complex structural imaging applications, particularly for hydrocarbon exploration targeting gas-charged formations and fault structures that create high incidence angle reflections. In applications where parallel wave propagation predominates, such as near-surface exploration, straightforward geological feature detection, and shallow subsurface characterization, higher wrapping angles (60° to 75°) exhibit enhanced sensitivity to parallel waves and low-angle broadside waves.

These findings carry direct implications for practitioners seeking DAS reflection records comparable to conventional geophones. Wrapping angle selection must align with the target geology, as complex structural targets such as curved gas-charged sand channels or steeply dipping fault planes demand low-angle configurations (15°–30°) because these structures generate predominantly high-incidence broadside reflections. Sub-horizontal targets permit greater flexibility in angle selection. Cable coupling also deserves careful attention in field deployment. Previous study demonstrated that weak coupling disproportionately degrades HWF performance while leaving straight fibre data relatively unaffected, making proper ground contact essential when deploying helical cables (Hendi *et al*., 2020). It is equally important to recognize that DAS remains a single-component measurement system regardless of wrapping configuration. The helical geometry redistributes sensitivity across incidence angles but does not replicate true three-component recording. For surveys requiring comprehensive wavefield characterization, HWF serves as a cost-effective complement to multi-component geophone arrays rather than an outright replacement. The inverse relationship between broadside and parallel wave sensitivity means that optimizing for one compromises the other, and survey planners must weigh these trade-offs against their specific imaging objectives before committing to a particular cable specification.

CONCLUSION

This study demonstrates that helically wound fibre (HWF) wrapping angles significantly impact distributed acoustic sensing (DAS) imaging capabilities for subsurface structure detection. HWF configurations with lower wrapping angles (15° and 30°) achieve quality comparable to conventional seismic vertical components (Vz) and offer better imaging performance for gas-charged sand channel features. These configurations successfully capture gas-charged sand channel features due to enhanced broadside sensitivity of 46.7% and 37.5% respectively at $\theta = 90°$ (calculated using Equation 2 from Kuvshinov, 2016). Conversely, higher wrapping angles (60° and 75°) exhibit gradually degraded performance with reduced broadside sensitivity of 12.5% and 3.34% respectively, approaching straight fibre characteristics and fail to capture reflections of the gas-charged sand channel.

The results reveal that choosing a wrapping angle is a trade-off between parallel wave detection capabilities and broadside wave sensitivity. Lower wrapping angles (15°-30°) are optimal for complex structural imaging that generates high incidence angle reflections. Higher wrapping angles (60°-75°) are suitable for near-surface application and simple geological feature detection where parallel and low incidence wave propagation dominates. To advance practical DAS deployment in exploration geophysics, this study fills important knowledge gaps by offering comparative evaluation across the entire range of practically feasible wrapping angles (15°-75°) and crucial guidance in choosing the best helical configurations based on particular geological targets.

This study also fills a practical gap in DAS research. Previous investigations have typically focused on individual wrapping angle configurations without providing comparative analysis for subsurface imaging applications, leaving practitioners and cable manufacturers with limited guidance when selecting optimal configurations for specific survey objectives. Our systematic evaluation across the complete range of practically feasible wrapping angles (15°-75°) offers the comparative framework that has been absent from the literature. From a practical standpoint, low-angle HWF configurations (15°-30°) demonstrate imaging quality comparable to conventional seismic vertical components, positioning them as viable alternatives for marine reflection surveys targeting complex geological features such as gas-charged formations. These findings strengthen the case for DAS technology as a cost-effective option in exploration geophysics where conventional seismic methods have traditionally dominated.

ACKNOWLEDGEMENT

The authors express their sincere gratitude to Universiti Teknologi PETRONAS and the Centre for Subsurface Imaging (CSI) for providing the research facilities and financial support that enabled this study. We gratefully acknowledge Total Energies for financial support through Grant cost-centre 015MD0-164. We also thank the reviewers for their constructive comments that improved the quality of this manuscript.

AUTHORS CONTRIBUTION

RRD: Conceptualize, methodology, data processing, formal analysis, visualization, writing – original draft preparation. SNFJ: Supervision, writing – review and editing. KAMN: Supervision, writing – review and editing. ARMA: Supervision, data processing, data imaging, review the results.

CONFLICT OF INTEREST STATEMENT

The authors declare that they have no known competing financial interests or personal relationships that could have influenced the work reported in this paper.

REFERENCES

Adeniyi, B.A., Abdul Latiff, A.H., Adedeji, Z.O., Md Arshad, A.R., & Asfha, D.T., 2025. Directional sensitivity of fibre optic cables for surface seismic reflection distributed acoustic sensing: a review and potential solutions for enhanced sensitivity. Geomechanics and Geophysics for Geo-Energy and Geo-Resources, 11, article no 60. https://doi.org/10.1007/s40948-025-00972-0.

Al Hasani, M., & Drijkoningen, G., 2023. Experiences with distributed acoustic sensing using both straight and helically wound fibers in surface-deployed cables—A case history in Groningen, The Netherlands. Geophysics, 88, B369-B380.

Asfha, D.T., Latiff, A.H.A., Otchere, D.A., Tackie-Otoo, B.N., Babikir, I., Rafi, M., Riyadi, Z.A., Putra, A.D., & Adeniyi, B.A., 2024. Mechanisms of sand production, prediction–a review and the potential for fiber optic technology and machine learning in monitoring. Journal of Petroleum Exploration and Production Technology, 14, 2577-2616.

Baird, A., 2020. Modelling the response of helically wound DAS cables to microseismic arrivals. First EAGE workshop on fibre optic sensing, 2020, 1-5.

Bakulin, A., Silvestrov, I., & Pevzner, R., 2020. Surface seismics with DAS: An emerging alternative to modern point-sensor acquisition. The Leading Edge, 39, 808-818.

Bellefleur, G., Schetselaar, E., Wade, D., White, D., Enkin, R., & Schmitt, D. R., 2020. Vertical seismic profiling using distributed acoustic sensing with scatter-enhanced fibre-optic cable at the Cu–Au New Afton porphyry deposit, British Columbia, Canada. Geophysical Prospecting, 68, 313-333.

Chen, Y., Zong, J., Liu, C., Cao, Z., Duan, P., Li, J., & Hu, G., 2023. Offshore subsurface characterization enabled by fiber-optic distributed acoustic sensing (DAS): An East China Sea 3D VSP survey example. Frontiers in Earth Science, 11, 1033456.

Chugaev, A., & Kuznetsov, A., 2023. Evaluation of the capabilities of distributed acoustic sensing with a helical fiber for cross-well seismic survey. Instruments and Experimental Techniques, 66, 868-874.

Chugaev, A., & Tarantin, M., 2023. Amplitude-frequency response of a helically-wound fiber distributed acoustic sensor (DAS). Mining Science and Technology (Russia), 8, 13-21.

Fernández-Ruiz, M.R., Soto, M.A., Williams, E.F., Martin-Lopez, S., Zhan, Z., Gonzalez-Herraez, M., & Martins, H.F., 2020. Distributed acoustic sensing for seismic activity monitoring. Apl Photonics, 5, 030901. https://doi.org/10.1063/1.5139602.

Hendi, S., Gorjian, M., Bellefleur, G., Hawkes, C.D., & White, D., 2020. Investigation of the Effects of Surrounding Media on the Distributed Acoustic Sensing of Helically-Wound Fiber-Optic Cable with Application to the New Afton Deposit, British Columbia. Solid Earth Discussions, 2020, 1-31.

Hornman, J., 2017. Field trial of seismic recording using distributed acoustic sensing with broadside sensitive fibre-optic cables. Geophysical Prospecting, 65, 35-46.

Kuvshinov, B., 2016. Interaction of helically wound fibre-optic cables with plane seismic waves. Geophysical Prospecting, 64, 671-688.

Martin, G.S., Wiley, R., & Marfurt, K.J., 2006. Marmousi2: An elastic upgrade for Marmousi. The Leading Edge, 25, 156-166.

Masaya, S., Tani, M., Liu, Y., & Tsvankin, I., 2024. Comparison of straight and helical fibers for time-lapse elastic FWI of synthetic seafloor DAS data. The Leading Edge, 43, 757-764.

Masoudi, A., & Newson, T.P., 2016. Contributed Review: Distributed optical fibre dynamic strain sensing. Review of scientific instruments, 87(1), 011501. https://doi.org/10.1063/1.4939482.

Mateeva, A., Lopez, J., Potters, H., Mestayer, J., Cox, B., Kiyashchenko, D., Wills, P., Grandi, S., Hornman, K., & Kuvshinov, B., 2014. Distributed acoustic sensing for reservoir monitoring with vertical seismic profiling. Geophysical Prospecting, 62, 679-692.

Muanenda, Y., 2018. Recent advances in distributed acoustic sensing based on phase-sensitive optical time domain reflectometry. Journal of Sensors, 2018, 3897873.

Noh, K.A.M., Harith, Z.Z.T., & Ab, A.H., 2015. Hybrid Source-Receiver Geometry for Short-Spread Layout in 2D Seismic Reflection Acquisition. In: Proceedings of the Petroleum Geoscience Conference & Exhibition 2015, Kuala Lumpur.

Pastor-Graells, J., Martins, H., Garcia-Ruiz, A., Martin-Lopez, S., & Gonzalez-Herraez, M., 2016. Single-shot distributed temperature and strain tracking using direct detection phase-sensitive OTDR with chirped pulses. Optics Express, 24, 13121-13133.

Pendão, C., & Silva, I., 2022. Optical fiber sensors and sensing networks: Overview of the main principles and applications. Sensors, 22, 7554.

Rafi, M., Mohd Noh, K.A., Abdul Latiff, A.H., Otchere, D.A., Tackie-Otoo, B.N., Putra, A.D., Riyadi, Z.A., & Asfha, D.T., 2024. Application of distributed acoustic sensing in geophysics exploration: Comparative review of single-mode and multi-mode fiber optic cables. Applied Sciences, 14, 5560.

Rashid, A., Tackie-Otoo, B.N., Abdul Latiff, A.H., Otchere, D.A., Jamaludin, S.N.F., & Asfha, D.T., 2025. Research Advances on Distributed Acoustic Sensing Technology for Seismology. Photonics, 12(3), 196. https://doi.org/10.3390/photonics12030196.

Tsuji, S., Araki, E., Matsumoto, H., Machida, Y., & Yokobiki, T., 2025. Relationship between surface ground motion and strain observed by a helically wound fiber-optic cable. Earth, Planets and Space, 77, 22.

Willis, M.E., 2022. Distributed acoustic sensing for seismic measurements–what geophysicists and engineers need to know. Society of Exploration Geophysicists. 162 p. ISBN 9781560803843.

Wuestefeld, A., & Wilks, M., 2019. How to twist and turn a fiber: Performance modeling for optimal DAS acquisitions. The Leading Edge, 38, 226-231.

Yavuz, S., Freifeld, B., Pevzner, R., Dzunic, A., Ziramov, S., Bóna, A., Correa, J., Tertyshnikov, K., Urosevic, M., & Robertson, M., 2019. The initial appraisal of buried DAS system in CO2CRC Otway Project: the comparison of buried standard fibre-optic and helically wound cables using 2D imaging. Exploration Geophysics, 50, 12-21.

Zhu, T., Shen, J., & Martin, E.R., 2020. Sensing earth and environment dynamics by telecommunication fiber-optic sensors: An urban experiment in Pennsylvania USA. Solid Earth Discussions, 2020, 1-30.

Ziramov, S., Young, C., Kinkela, J., Turner, G., & Urosevic, M., 2023. Pre-stack depth imaging techniques for the delineation of the Carosue Dam gold deposit, Western Australia. Geophysical Prospecting, 71, 1077-1095.

Manuscript received 2 October 2025;
Received in revised form 6 January 2026;
Accepted 26 February 2026
Available online 27 November 2026